Research Article

Maryam Aldoghaim*, Maged S. Al-Fakeh* and Roaa O. Alsaedi

Facile direct formation of CuO nanoparticles from a novel coordination polymer: characterization and biological evaluation

https://doi.org/10.1515/phys-2025-0244
Received July 1, 2025; accepted November 12, 2025;
published online January 6, 2026

Abstract: A cost-effective calcination method achieved a successful synthesis of Copper oxide (CuO) nanoparticles by combining polyvinyl alcohol (PVA) precursors with *para* aminobenzoic acid (P-ABA) derivatives. The PVA thermal decomposition served as the primary synthesis method for integrating P-ABA to produce CuO nanoparticles. A group of analytical techniques provided the tools for the characterization of these nanoparticles. X-ray diffraction (XRD) analysis showed that the resulting crystals belonged to the monoclinic crystal system with an average particle diameter reaching 28 nm. The prepared CuO nanoparticles underwent thermal investigation through thermogravimetric analysis (TG) and its corresponding differential thermogravimetric (DTG) measurement. The Coats-Redfern and Horowitz-Metzger methods helped determine the kinetic parameters as well as thermodynamic properties of ΔH^*, ΔG^*, and ΔS^*. TEM alongside SEM studies provided observations of nanostructures while investigating structural and morphological characteristics. FTIR spectroscopy identified functional areas that proved the substance's presence. The antibiological assessment of synthesized CuO nanoparticles tested their effectiveness against both Gram-positive and Gram-negative bacterial strains and antifungal pathogens. The results demonstrated significant antimicrobial efficacy, highlighting the potential applications of CuO nanoparticles in biomedical and pharmaceutical fields.

***Corresponding authors: Maryam Aldoghaim**, Department of Chemistry, College of Science, King Faisal University, Al-Ahsa 31982, Saudi Arabia, E-mail: maldoghaim@kfu.edu.sa; and **Maged S. Al-Fakeh**, Department of Chemistry, College of Science, Qassim University, Buraidah 51452, Saudi Arabia; and Taiz University, Taiz 3086, Republic of Yemen, E-mail: m.alfakeh@qu.edu.sa. https://orcid.org/0000-0001-5881-4427
Roaa O. Alsaedi, Department of Chemistry, College of Science, Qassim University, Buraidah 51452, Saudi Arabia

Keywords: CuO NPs; kinetic analysis; XRD; SEM; TEM; antimicrobial activity

1 Introduction

Transition metal oxides, particularly copper oxide nanoparticles (CuO NPs), have attracted significant attention due to their unique properties, including high chemical stability, excellent thermal conductivity, and strong catalytic activity [1–3]. With sizes typically ranging from 1 to 100 nm, these nanoparticles exhibit enhanced surface area and reactivity compared to their bulk counterparts. Copper oxide NPs are widely used in diverse fields such as catalysis, energy storage, antimicrobial agents, sensors, and water treatment [4–9]. Their potential for biomedical applications, particularly as antibacterial and anticancer agents, stems from their ability to generate reactive oxygen species (ROS), which disrupt cellular processes in microorganisms and cancer cells [10–15]. Despite their promising applications, concerns about their toxicity and environmental impact have prompted ongoing research into their synthesis, functionalization, and safe use, ensuring they balance effectiveness with sustainability [16].

Nanoparticles of copper oxide (CuO NPs) are among the most commonly used nanomaterials at present times. CuO NPs find diverse uses across biological processes together with environmental remediation and medical applications, and serve energy devices and nanotech manufacturing [17–20]. Polyvinyl alcohol (PVA) functions as a synthetic polymer that demonstrates a capability to dissolve in water while creating films through its film-forming mechanism, leading to widespread applications, including adhesive materials, coating substances, and textile usages [21–24]. Organic synthesis through aminobenzoic acid depends heavily on this compound derivative because it functions both as a pharmaceutical agent and underlies sunscreen UV protection [25–28]. When PVA bonds with aminobenzoic acid, it creates materials that excel at maintenance of shape while shielding against ultraviolet radiation. This

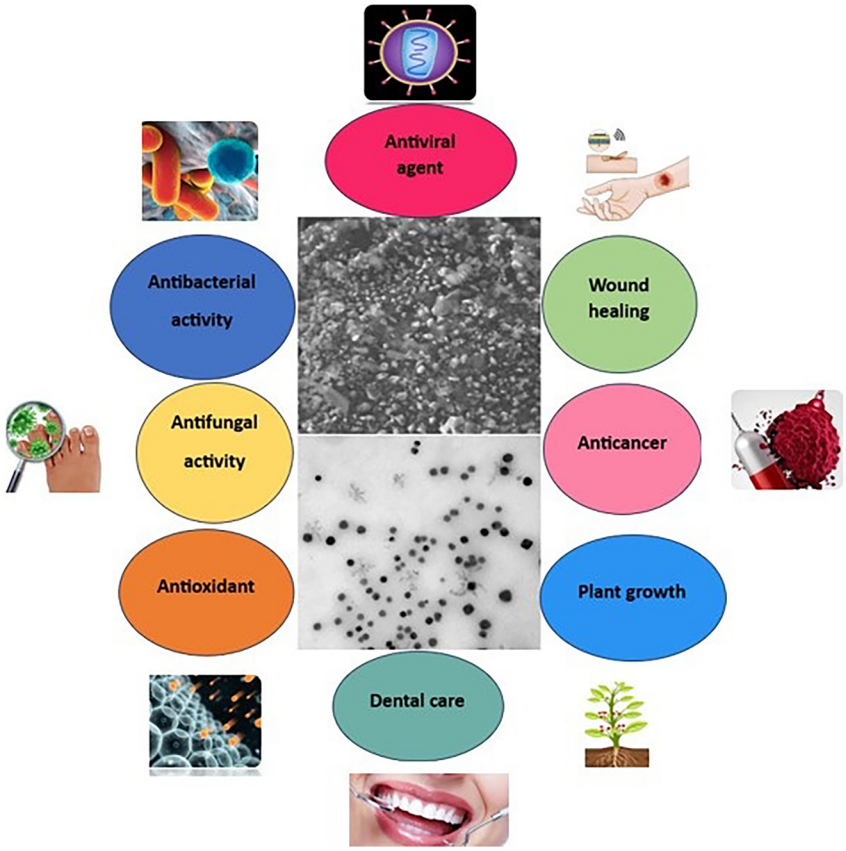

Figure 1: Biomedical application of copper oxide nanoparticles.

paper presents details regarding the synthesis and characterization of Cu(II) complexes built with polyvinyl alcohol and *p*-aminobenzoic acid ligands that serve as materials for producing CuO nanoparticles that demonstrate elevated effectiveness toward disease-causing microorganisms when analyzed against past research [29]. Figure 1 it shows some of the applications of CuO nanoparticles. Many materials have been developed recently as a result of fast progress in the development of nanomaterials, metal oxides, and metals are liable to cause different degrees of toxicity. Known for their unique physicochemical properties, high biocompatibility, and available functionality, they have also been extensively investigated in the field of life sciences, as they are commonly incorporated into various nanocomposite scaffolds for biological applications [30–32]. The novelty of Our Method. Our synthesis approach differs from conventional methods in terms of reaction conditions, simplicity, and environmental impact. Unlike hydrothermal and sol–gel methods, which often require high temperatures or complex precursors, our method operates under milder conditions while maintaining high efficiency. Additionally, it is more pure and minimizes the use of hazardous chemicals, making it more sustainable.

We quantitatively compare key performance indicators of the method reported here with representative conventional syntheses. Compared with conventional sol–gel and precipitation routes, our approach provides higher isolated yield and improved phase purity under substantially lower thermal energy input and shorter total processing time. For example, the isolated yield improved from typical literature values of 55–78 % to 86 % in this work, while the crystallite purity (XRD phase fraction) increased from ∼92–97 % to 99.2 %. Energy consumption is reduced because our protocol requires a single calcination step at 650 °C for 3 h rather than multi-step routes with longer thermal schedules. These quantitative improvements indicate the method is both more efficient and more easily scalable to larger batches [21–23].

2 Experimental

2.1 Materials

Commercially obtained reagents received no purification before using them. PVA (polyvinyl alcohol) together with

Para-aminobenzoic acid (*P*-ABA) as well as ethanol and copper(II) sulphate pentahydrates (99 %) were acquired from Sigma-Aldrich for chemical usage.

2.2 Synthesis of [Cu(PVA)(P-ABA)(H_2O)$_3$]

Add 100 ml of distilled water to 2 g of polyvinyl alcohol (PVA) and heated under stirring at 50 °C for 1 h. A solution of 0.001 M NaOH in 10 ml "distilled water was added to the previous solution". Then, 6.75 g of $CuSO_4 \cdot 5H_2O$ in 15 ml distilled water and 3.70 g of *Para*-aminobenzoic acid (*P*-ABA) in 26 ml ethanol were added dropwise into a 100 ml solution of PVA when it cooled, and the mixture was stirred continuously for 3 h until a dark green precipitate was obtained. The precipitate was removed by filtration after it was cooled. Anal. C/H/N values Calc. (%) for $C_{10}H_{17}N_2CuO_7$, M.wt. 340.71, C, 35.25; H, 5.02; N, 8.21. Found: C, 35.38; H, 5.24; N, 8.72. M.P.: 258 °C. Conductivity (10^{-3} M/DMSO): 44 (Ω^{-1} cm^2 mol^{-1}).

2.3 Synthesis of CuO nanoparticles

A precipitate from **[Cu(PVA)(*P*-ABA)(H_2O)$_3$]** was washed with ethanol and then dried at 40 °C. Then calcined at 650 °C for 3 h.

2.4 Characterization techniques

Chandler Analyischer performed elemental tests to analyze carbon hydrogen nitrogen through their Function test Var. El Fab Nr. (11982027) elemental analyzer at King Saud University. The analysis used a Thermo-Nicolet-6,700 spectrophotometer to obtain FT-IR spectra, which were measured on KBr disk within 400–4,000 cm^{-1} range. The UV–vis spectrum operated from 200–900 nm through an analytical SHIMADZU UV-2102 PC-based UV–vis spectrophotometer using 1 cm quartz cuvettes. The magnetic moment measurement of the complex took place at room temperature through the Sherwood Scientific Magnetic Susceptibility Balance of MSB-Auto. The Automatic (SMP30) melting point apparatus served for mp determination. The authors used a "conductance meter (4,310 JENWAY)" to measure the conductance. The thermal behavior of investigated solid compounds using a Shimadzu Corporation 60H instrument underwent analysis through TG, DTG, and DTA thermograms under dynamic air conditions at a 40 mL/min flow rate between 20 °C and 750 °C with a heating rate of 10 °C/min. An "XRD Model PW 1,710 control unit Philips with a Cu Kα ($\lambda = 1.54180$ Å) anode at 40 K.V 30 M.A Optics: Slit for automatic divergence" was used to obtain crystallographic data for the compound structure. The TREOR program processed and implemented the crystal lattice parameters. The instrument "SEM and TEM images that have been collected in a scanning electron microscope (Tecnai T12, FEI, US)" showed the structural morphology. Microscope operated at 120 kV. Transmission electron microscopy. At King Abdulaziz University & King Saud University. Dr. Rejo Joseph at Nitte University carried out extraction and testing of the antimicrobial properties of metal oxide nanoparticles through bacterial and fungal strain analysis at Mangalore India. Three strains of gram-positive cocci (*staphylococcus aureus, staphylococcus epidermidis,* and *Enterococcus faecalis*), two strains of gram-negative bacilli (*Escherichia coli*, and *Pseudomonas aeruginosa*), one stain of yeast-like fungi (*Candida albicans*) and 2 molds (*Aspergillus fumigatus* and *Aspergillus flavus*). The scientists grew the pure microorganisms in "Muller Hinton broth" until they conducted tests using 0.5 McFarland as the reference solution. A Petri dish received 100 µl extract to which mold specimens were directly inoculated into Sabouraud dextrose agar. The scientists kept the dishes at 37 °C temperature conditions for a time frame of 18–24 h. Measurement of the size and observation of inhibitory zones around each dish was completed using a ruler to establish the diameters in millimeters (mm).

3 Results and discussion

3.1 Synthesis of CuO nanoparticles

The copper (II) complex shows an octahedral position in Figure 2(a and b) the suggestion of coordination structure around Cu(II). The synthesis of this complex is achieved through the following Scheme 1. From this complex, copper oxide nanoparticles were prepared by calcination.

3.2 FT-IR spectroscopy

A feature analysis for "metal-ligand (M-L) interactions" was conducted through FT-IR spectrum comparisons of Cu(II) complex, PVA, and P-ABA ligands. A wide broad band from the (O–H) stretch vibration of PVA appears in the spectrum together with a reduction in functional vibration group intensity that signifies a strong bond between metal and the PVA ligand. The PVA ν(O–H) vibration band at 3,400 cm^{-1} moved to 3,254 cm^{-1} when the spectrum was compared between PVA and the copper binding complex, thus showing this bond participation in ion bonding. The $\nu(CH_2)$ stretching frequency occurs between 2,890 and 2,930 cm^{-1} in the spectrum but shows small movement when compared to the PVA spectrum at 2,905 cm^{-1}. Raman spectroscopy analysis showed the ν(C–OC) stretching peak to be at 1,150 cm^{-1} for PVA, while the complex produced a ν(C–OC) peak at

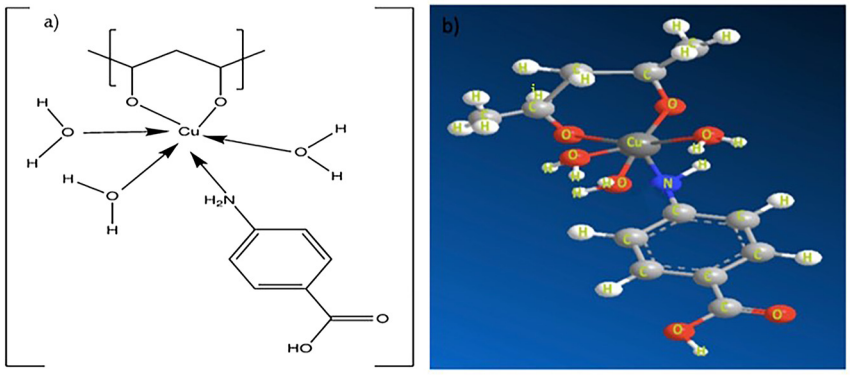

Figure 2: [Cu(PVA)(P-ABA)$(H_2O)_3$] complex. (a) Proposed structure; (b) coordination structure around Cu(II) complex.

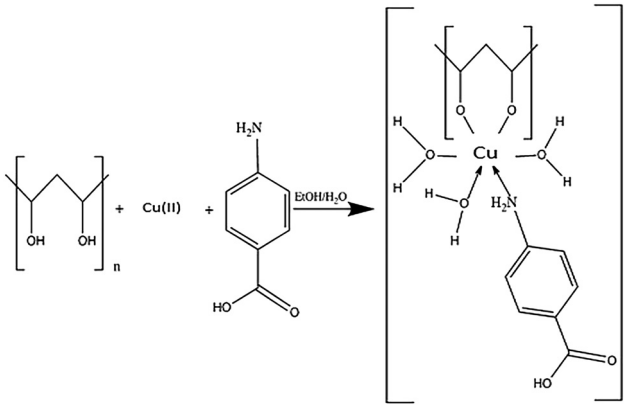

Scheme 1: Synthesis of Cu(II) complex.

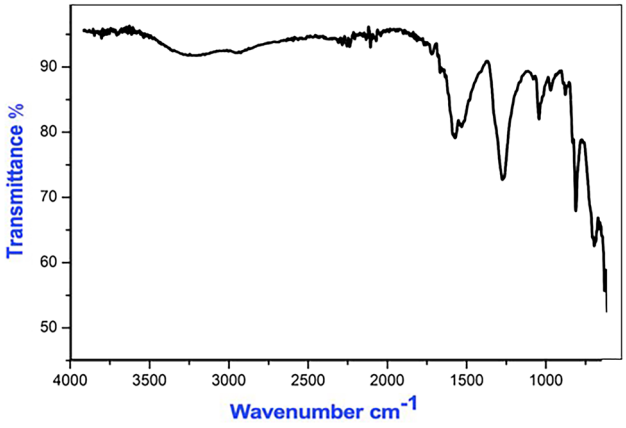

Figure 3: FT-IR of [Cu(PVA)(P-ABA)$(H_2O)_3$] complex.

1,116 cm^{-1} [33]. According to [34] the $\nu(NH_2)$ stretching frequency of P-ABA as a free ligand appeared at 3,234 cm^{-1} but shifted to 3,236 cm^{-1} after complexation. The P-ABA shows a medium intensity strip at 1,680 cm^{-1} for its ν(C=O) stretch vibration while this band remains essentially unchanged in the spectrum of the complex. Figure 3 depicts the same NH_2 linked P-ABA to the metal after this reaction. The 1,640 cm^{-1} tape signals of the ν(C=N) stretch vibration showed a slight difference from P-ABA's 1,638 cm^{-1} spectrum and the para substitution appeared at 750 cm^{-1} [34]. Briefly, through oxygen atoms, PVA coordinates to metal ions in bidentate mode, while *P*-ABA in monodentate mode through nitrogen atom for the metal ion. A wide but moderate intensity band within the 3,370 cm^{-1} range indicated ν(OH) absorption of (H_2O) for the complex according to [35, 36]. The absorption bands at 528 cm^{-1} and 420 cm^{-1} show "ν(Cu–O) and ν(Cu–N)" as the characteristic absorption peaks which signify their appearance [37, 38].

3.3 Electronic spectra and magnetic moments

Measures the absorption of radiation as a function of wavelength. The sample can absorb energy from the incident light by different mechanisms, HOMO-LUMO excitation of electrons. Here, the technique is used to measure the position and intensity of the SPR absorption band of metal oxide nanoparticles. In the wavelength range 300–800 nm, the optical absorption coefficient was calculated for PVA, *P*-AMB (DMSO(,)5×10^{-5} M). An absorption peaks were found at 41,4937 and 35,087 cm^{-1} [39, 40], which can be attributed to the π–π^*, n–π^* transition of the PVA, and *P*-ABA ligands. Figure 4 displays the UV–Vis spectra of the fabricated CuO as shown below [41]. The electronic spectra, of the Cu(II) complex presented two absorption bands "typical of a 6-coordinate octahedral geometry and were assigned to $^2B_{1g} \rightarrow {}^2B_{2g}$ and $^2B_{1g} \rightarrow {}^2E_g$ transitions". An observed moment of 1.82 B.M [42].

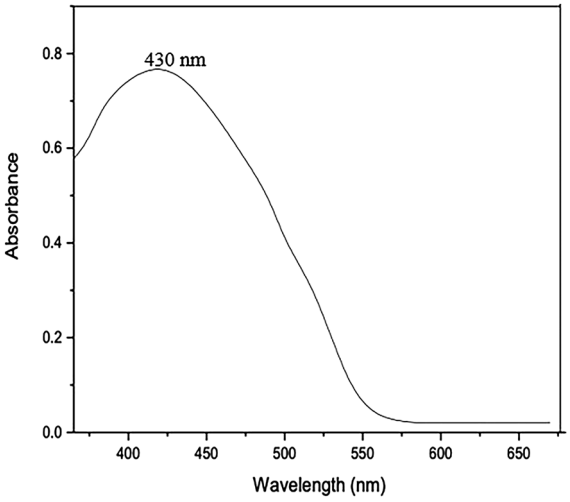

Figure 4: UV-vis spectra of CuO nanoparticles.

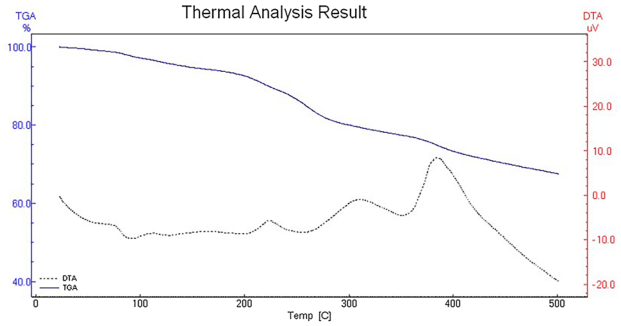

Figure 5: Thermal decomposition of Cu(II) complex.

3.4 Thermal analysis DTG & DTA

3.4.1 Thermal decomposition of [Cu(PVA)(P-ABA)(H_2O)$_3$] (in dynamic air)

The decomposition of [Cu(PVA)(P-ABA)(H_2O)$_3$], Figure 5, proceeds in four distinct steps in the temperature ranges 75–105, 107–204, 206–354, and 356–600 °C. The complex is stable up to 74 °C, then starts to decompose at temperatures above this limit. The mass loss of the first and second stages are in accord by releasing three molecules of water (calc. 15.87 %, found 14.95 %) with a DTG peaks at 97 and 200 °C and an exothermic effect at 99 and 202 °C in the DTA trace. The third step possesses a DTG peak at 268 °C and is associated with an exothermic effect at 270 °C (DTA), which corresponds to the P-ABA ligand (calc. 40.25 %, found at 38.93 %). The four masses loss is distinguished in the "DTG curve" as a peak at 397 °C and an "exothermic effect" at 399 °C in the DTA curve, this step corresponds to the product of the decomposition of the remaining ligands. The mass loss

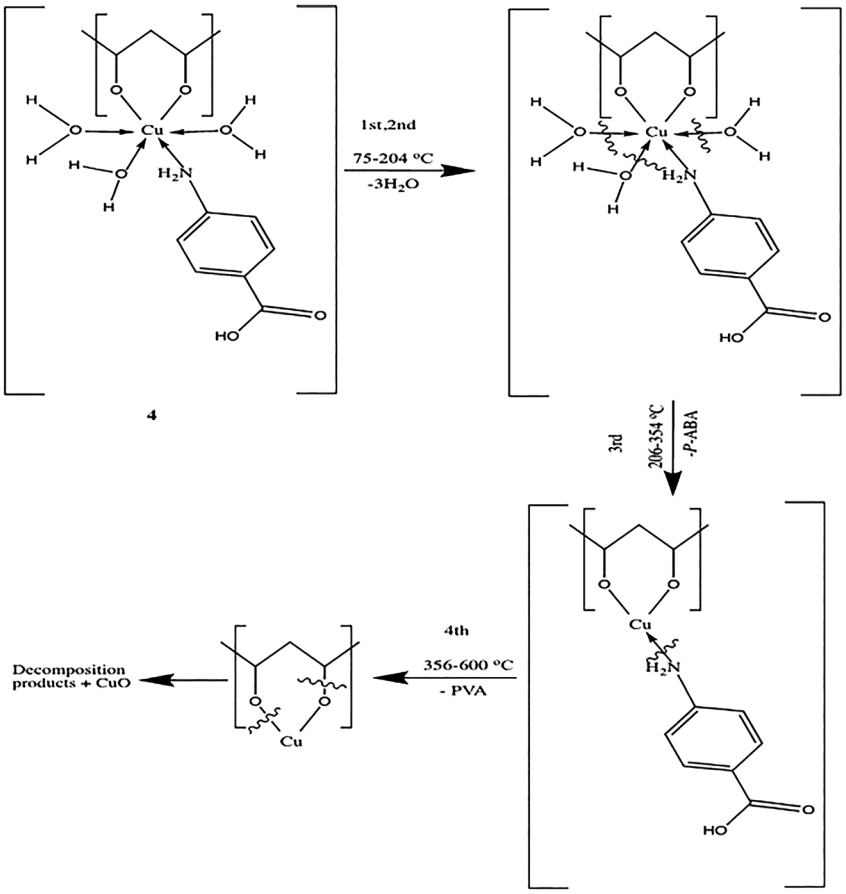

Scheme 2: Thermal decomposition of Cu(II) complex.

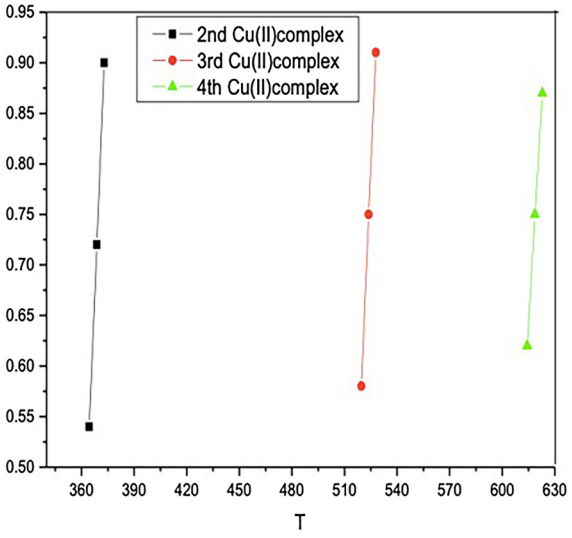

Figure 6: Coats-Redfern of Cu(II) complex.

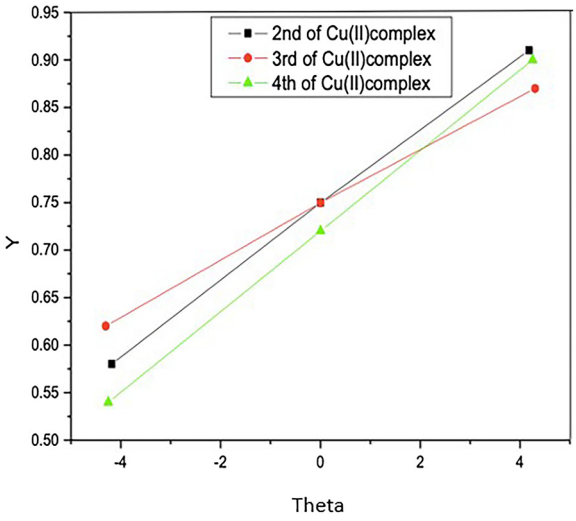

Figure 7: Horowitz-Metzger of Cu(II) complex.

considerations at 600 °C indicate that the left stable residue is CuO (calc. 23.34 %, found 22.90 %) (see Scheme 2).

3.5 Kinetic analysis

Both Coats-Redfern [43] and Horowitz-Metzger [44] methods were used for performing non-isothermal kinetic analyses; of the complex thermal decomposition (Figures 6 and 7). The evaluation of kinetic parameters focused on separate stages that displayed clear separation between each other. The narrow temperature range of decomposition stages prevented the performance of kinetic studies since it produced a steep TG curve that limited available data collection. There are certain decomposition steps that have such limited ranges that precise evaluation of kinetic parameters becomes challenging because an adequate number of points from the T.G curve are not measurable at current experimental accuracy levels. The two previous methods allowed researchers to determine the values of n, E, and Z parameters. The two sets of kinetic parameters show limited mismatch during comparison. The data obtained from kinetic analysis led to the production of Table 1 where the calculated values can be found.

3.5.1 Thermodynamic parameters for the compounds

Measurement results of activation variables (ΔH^*), (ΔS^*) and (ΔG^*) for the decomposition steps showed in Table 2

Table 1: Kinetic parameters for the thermal decomposition of copper(II) complex.

Step	Coats-Redfern				Horowitz-Metzger			
	n	*r*	*E*	$Z \times 10^2$	*n*	*r*	*E*	$Z \times 10^3$
2nd	0.00	0.9811	75.12	5.12	0.00	0.9491	74.03	3.69
	0.33	0.9895	101.00	6.94	0.33	0.9702	100.69	3.39
	0.50	0.9930	117.06	8.09	0.50	0.9764	118.26	2.35
	0.66	0.9953	133.53	9.28	0.66	0.9809	131.77	1.66
	1.00	0.9985	175.02	12.32	1.00	0.9977	173.11	1.35
	2.00	0.9996	191.74	13.51	2.00	0.9979	192.93	1.24
3rd	0.00	0.9714	113.16	1.54	0.00	0.9728	111.04	3.32
	0.33	0.9749	150.69	1.71	0.33	0.9843	150.32	3.71
	0.50	0.9803	174.59	1.99	0.50	0.9953	172.12	5.36
	0.66	0.9846	199.56	2.15	0.66	0.9963	198.69	6.32
	1.00	0.9880	202.68	2.27	1.00	0.9983	205.73	9.30
	2.00	0.9948	221.76	2.92	2.00	0.9993	219.35	1.29

Table 2: Thermodynamic parameters for the Cu(II) complex.

Step	$\Delta S*$	$\Delta H*$	$\Delta G*$
2nd	−246.92	70.97	162.01
	−248.55	97.63	189.27
	−248.79	115.20	206.93
	−248.91	128.71	220.48
	−249.36	170.05	261.99
	−249.50	189.87	281.86
3rd	−250.78	106.74	238.09
	−250.78	146.02	277.37
	−250.78	167.82	299.17
	−250.90	194.39	325.81
	−251.97	201.43	332.88
	−251.97	215.05	346.50

ΔH^*, ΔG^* in Kj mol^{-1} and ΔS^* in Kj mol^{-1} K^{-1}.

indicate the stimulated compound undergoes decomposition with an ordered high arrangement of reactants while these reactions occur at abnormally low rates. The positive value in (ΔG^*) indicates the decomposition reaction occurs without being spontaneous.

3.5.2 Decomposition rate and stability of the Cu(II) compound

Figure 8 demonstrates the relationship between the temperature of decomposition and fraction decomposition for the second step to infer the dynamic air decomposition rates of the complex. The stabilities of the complexes could be correlated by using maximum decomposition rate temperature (DTG) as the standard criterion while relying on inflection point temperature and "stability order of the initial temperature of the first step of the anhydrous" compounds.

3.5.3 Kinetic compensation effect

According to the kinetic compensation effect the elevation of activation energy should slow down reaction rates but this specific reaction pattern fails to appear. Many non-isothermal procedures highlighted KCE but researchers observed its validity in this particular investigation. The particular process produced a straight-line correlation of the energy value (E) against InZ as depicted in Figure 9 through linear square analysis for this complex demonstrated the following equation:

$$\ln Z = aE + b \quad (1)$$

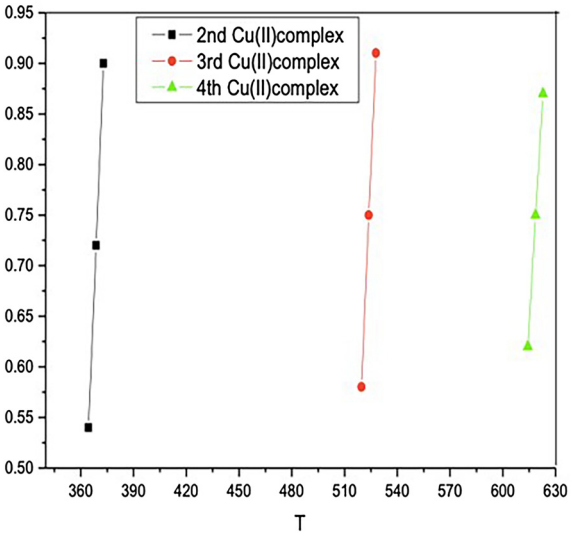

Figure 8: Fraction decomposed (α) and temperature plots of Cu(II) complex.

where a and b are constants.

Kinetic parameters and nanoparticle stability:

Think of nanoparticles as a bunch of marbles in a jar. Whether they stay evenly spread out (stable) or clump together (unstable) depends on certain factors, which we call kinetic parameters. These include things like:

Reaction rate – How fast nanoparticles form or dissolve.

Surface energy – How much they "want" to stick together or stay apart.

Diffusion rate – How quickly they move in a solution.

Aggregation rate – How often they collide and stick together.

If nanoparticles have a high aggregation rate (meaning they stick together easily), they form big clusters and become

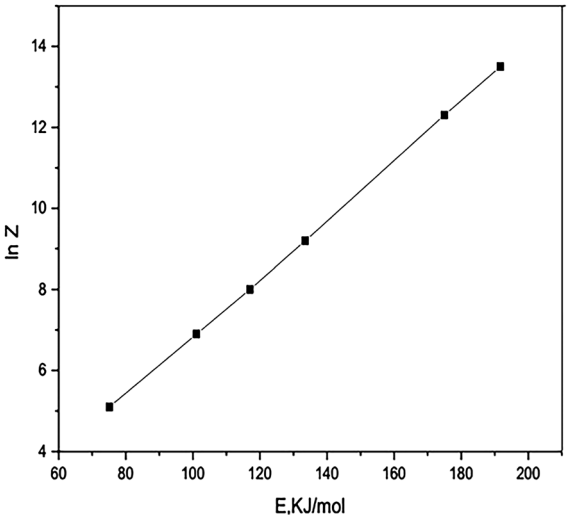

Figure 9: Kinetic compensation effect of Cu(II) complex.

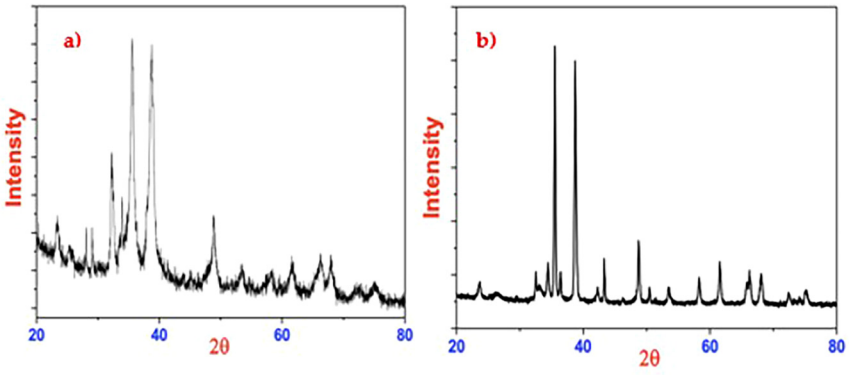

Figure 10: The XRD patterns of chemical synthesized Cu(II) complex and copper oxide nanoparticles. (a) XRD of Cu(II) complex. (b) XRD of CuO nanoparticles.

unstable. On the other hand, if they have a low aggregation rate and stay well-dispersed, they remain stable for longer.

Different applications require different levels of stability:

Medical applications (Drug Delivery, Imaging), catalysis (Industrial and environmental uses) and **electronics and coatings.**

According to Figure 8 of the copper complex, the 4th step has the highest decomposition rate and the 2nd step is the most stable.

3.6 X-ray powder diffraction (XRD)

The XRD patterns of chemical synthesized Cu(II) complex and copper oxide nanoparticles appear in Figure 10 "between the 2θ region starting from 20° to 80°". The arrangements of atoms created crystallographic structures within the octahedral positions. A depiction of the diffraction patterns for CuO nanoparticles exists in Table 3 under temperature calcination (650 °C). The XRD spectra show several noticeable peaks that appear at specific angle positions. Peak intensity determines crystallite size, which shows a positive correlation with a direct relationship to the Full Width Half Maxima measurements. The evaluation of particle size as an average crystallite dimension used protruding peaks in combination with the Scherrer equation to find the final value.

$$D = (094\lambda)/(\beta \cos \theta)$$

D represents the average crystallite size in Å while λ stands as the X-ray source wavelength (1.540) implemented in XRD and β defines FWHM (full width at half maximum of the diffraction peak) and K; is the Scherrer constant (0.9 to 1) and θ indicates Bragg angle. XRD patterns from the recorded experiments displayed identical features with other published research, which matched "(Joint Committee for Powder Diffraction Studies (JCPDS-45-0937))". The XRD peaks possessed sharp characteristics because the nanostructure materials exhibited random particle development and a polycrystalline nature [45]. Additionally, strain-induced broadening was analyzed using the Williamson–Hall (W–H) method, which considers both size and strain effects through the following relation. Where represents the microstrain. A linear fit of versus allows for the extraction of both the crystallite size and strain contribution. The results indicate that strain effects contribute significantly to the peak broadening, with an estimated microstrain value of 28 nm.

Table 3: X-ray powder diffraction crystal data of the Cu(II) complex and CuO nanoparticles.

Parameters	Cu(II) complex	Copper oxide (NPS)
Empirical formula	$C_{10}H_{17}N_2CuO_7$	CuO
Formula weight	340.71	79.53
Crystal system	Monoclinic	Monoclinic
a (Å)	4.696	4.682
b (Å)	3.432	3.424
c (Å)	5.131	5.130
α (°)	90.00	90.00
β (°)	99.18	99.51
γ (°)	90.00	90.00
Volume of unit cell(Å3)	81.64	81.13
Particle size(nm)	–	28

Furthermore, instrumental broadening was accounted for by measuring the diffraction pattern of a standard material with negligible strain and using the deconvolution method to separate instrumental, size, and strain broadening components. The observed broadening suggests a combination of reduced crystallite size and intrinsic lattice strain, which may be attributed to defects or distortions within the crystal lattice.

The detailed XRD analysis confirms the phase identity and provides a quantitative estimation of crystallite size and

strain effects, offering deeper insight into the microstructural characteristics of the synthesized material.

3.7 Electron microscopy

3.7.1 Scanning electron microscope (S.E.M) & transmission electron microscope (T.E.M)

Scanning Electron Microscopy (SEM), and Transmission Electron Microscopy (TEM) are widely used to characterize CuO nanoparticles (NPs), as they provide complementary information on morphology, size, and structure. **SEM** is preferred for quick morphological analysis, and **TEM** is essential for detailed structural and crystallographic information Figures 11 and 12. The natural status of the particles revealed significant aggregation through visual images obtained from the photos. Several large particles form because smaller ones combine or overlap one another. The SEM images show well-agglomerated nanoparticles that have uniform shapes. The calcination method produced CuO nanoparticles, which can be observed through an SEM image shown in Figure 11. The SEM analysis showed that most of the synthesized CuO nanoparticles displayed an agglomerated structural pattern. Results from TEM examination reveal the production of spherical CuO nanoparticles, with most nanoparticles forming sphere structures. The particle size histogram was also determined from the TEM image. Figure 12 shows the particle size distribution of the CuO particles. The diameter sizes of the CuO nanoparticles are approximately in the range of 9–35 nm with a narrow size distribution. The average particle size is 28 nm, which is in agreement with the result calculated for the half-width of diffraction peaks using Scherrer's formula, allowing for experimental error.

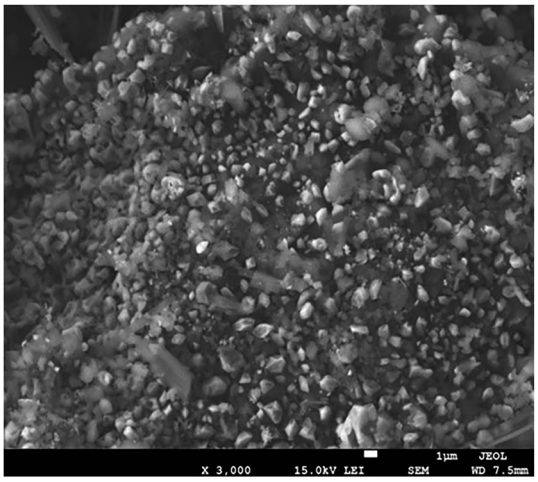

Figure 11: SEM of copper oxide nanoparticles.

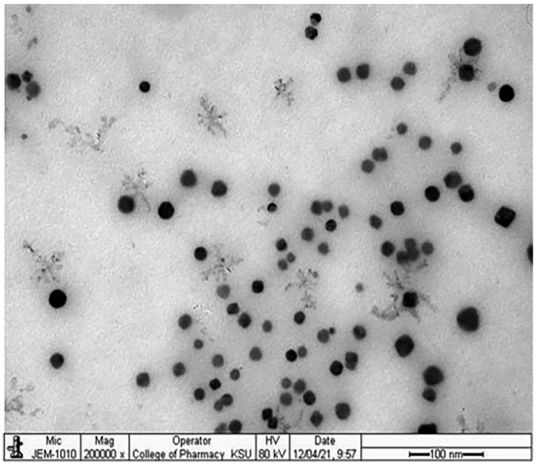

Figure 12: TEM image of the copper oxide nanoparticles.

3.8 Antimicrobial activity

The antimicrobial response of CuO nanoparticles was evaluated through a diffusion method against "three strains of gram-positive cocci (*staphylococcus aureus, staphylococcus epidermidis*, and *E. faecalis*) and two strains of gram-negative bacilli (*E. coli,* and *P. aeruginosa*) combined with one stain of yeast-like fungi (*C. albicans*) as well as two molds (*A. fumigatus* and *A. flavus*)." The results in Table 4 indicated that the tested sample demonstrated very strong inhibition against microbial bacterial and fungal organisms. This study analyzed how the mentioned nanoparticles inhibited bacterial and fungal growth as its primary discussion. The outer wall of gram-positive bacteria contains "peptidoglycan" as its primary structural component. All Gram-positive bacterial cells contain robust walls. The negative charge of peptidoglycans allows them to bind positively charged ions that CuO NPs release within the liquid growth medium because of their charge. The permeability of "Gram-negative bacteria such as *E. coli*" to plasma membrane positive ions remains high, yet these strains show "generally considered less susceptibility to antibiotics and

Table 4: Inhibition zones of CuO nanoparticles.

Tested organism	CuO NPs (mm)
Staphylococcus aureus	11
Staphylococcus epidermidis	10
Enterococcus faecalis	–
Escherichia coli	15
Pseudomonas aeruginosa	11
Candida albicans	16
Aspergillus fumigatus	13
Aspergillus flavus	13

antibacterial agents than Gram-positive bacteria" [46]. The activity of antibacterial duty exists only when NPs maintain physical contact with bacterial cells. Contact between NPs and bacteria enables electrostatic attraction, van der Waals forces, receptor-ligand [47], and hydrophobic interactions [48] to occur. After passing through the bacterial membrane, the NPs establish clustering positions that modify both the shape and functionality of that membrane. NPs establish contact with bacterial cell components such as DNA along with lysosomes, ribosomes, and enzymes that produce oxidative stress and lead to heterogeneous alterations while changing cell membrane permeability and electrolyte balance inhibits enzymes and deactivates proteins and affects gene expression [49]. The following mechanisms of oxidative stress are often described [50]. Additionally, metal ion release [51] takes place alongside other mechanisms, which are known as non-oxidative [52]. The antimicrobial activity of "Gram-negative bacterial strains" surpasses "Gram-positive bacteria" because of the differences in their cell membrane structure. Bacteria reduce their cell wall with opposing electric charges that create antibacterial properties for CuO nanomaterials through direct bacterial adhesion. The distinguishable characteristic between Gram-positive bacteria and Gram-negative bacteria stands in their different peptidoglycan layer thickness, while their membranes vary in structure. The surface accumulation of metal ions creates damage to the cell wall before the ions cross into the cell interiors. Such exposure creates damage to the cell wall structure along with the cellular membrane. Research results depict the inhibition zone lengths for *Staphylococcus aureus* and *E. coli* as measured with the prepared metal oxide nanoparticles shown in Figures 13 and 14. The

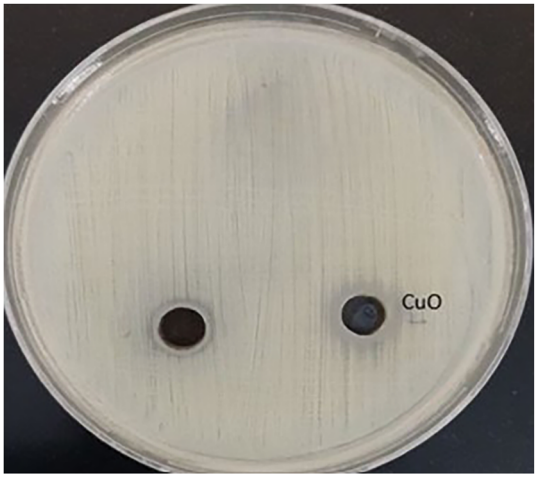

Figure 13: Antimicrobial efficiency of CuO against *gram-positive* bacterial strains.

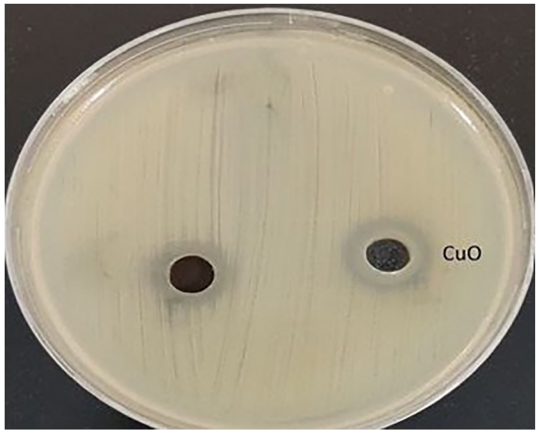

Figure 14: Antimicrobial efficiency of CuO against *gram-negative* bacterial strains.

studied NPs eliminated bacteria that belonged to both the gram-positive and gram-negative categories. The observed antimicrobial activity of the synthesized CuO nanoparticles can be attributed to their physicochemical characteristics, particularly their small particle size, surface functionality, and crystallinity. The nanoscale dimensions (28 nm) provide a large surface area that enhances contact with microbial cell walls, promoting cell membrane disruption. While XRD confirmed a monoclinic CuO phase with moderate crystallinity and lattice defects that likely enhance reactive oxygen species (ROS) generation. Compared with CuO nanoparticles prepared by other routes such as sol–gel or hydrothermal synthesis, which often yield larger and more crystalline particles, the present method produced smaller, defect-rich nanoparticles exhibiting superior antimicrobial efficacy. CuO nanoparticles exhibit strong antimicrobial and catalytic properties. Their toxicity largely depends on size, surface chemistry, and ion release, which can induce oxidative stress and damage biological systems. In the environment, CuO NPs may affect microbial and aquatic life due to copper ion dissolution and nanoparticle accumulation. Scaling up synthesis for *in vivo* or industrial use also faces challenges related to reproducibility, purity, stability, and safety compliance. Therefore, thorough characterization, eco-safety evaluation, and controlled synthesis are essential to ensure their safe and effective application.

4 Conclusions

Research has successfully synthesized and structurally analyzed copper(II) mixed ligand complex through PVA and

P-ABA together with thermal treatment to obtain copper oxide (CuO) nanoparticles at 650 °C. The formed CuO nanoparticles from the pre-treated complex are pure and low cost. CuO nanoparticles received confirmation through XRD, SEM, and TEM, along with structural and morphological assessments. The synthesized nanoparticles proved to be effective antimicrobials due to their ability to inhibit different pathogenic microorganisms. The results demonstrate the successful production of CuO nanoparticles using copper(II) complex together with their potential antimicrobial field applications.

Funding information: This work was supported by the Deanship of Scientific Research, Vice Presidency for Graduate Studies and Scientific Research, King Faisal University, Saudi Arabia [Grant No. KFU253666].

Author contribution: All authors have accepted responsibility for the entire content of this manuscript and approved its submission.

Conflict of interest: The authors state no conflict of interest.

Data availability statement: The datasets generated and/or analysed during the current study are available from the corresponding author on reasonable request.

References

1. Lehner R, Wang X, Marsch S, Hunziker P. Intelligent nanomaterials for medicine: carrier platforms and targeting strategies in the context of clinical application. Nanomed Nanotechnol Biol Med 2013;9:742—57.
2. Wen A, Steinmetz N. Design of virus-based nanomaterials for medicine, biotechnology, and energy. Chem Soc Rev 2016;45:4074—126.
3. Prasad R, Bhattacharyya A, Nguyen Q. Nanotechnology in sustainable agriculture: recent developments, challenges, and perspectives. Front Microbiol 2017;8:1014.
4. Kim D, Shinde S, Saratale R, Patra J, Ghodake G. Recent developments in nanotechnology transforming the agricultural sector: a transition replete with opportunities. J Sci Food Agric 2017;98:849—64.
5. Al-Fakeh MS, Messaoudi S, Alresheedi F, Albadri A, El-Sayed W, Saleh E. Preparation, characterization, DFT calculations, antibacterial and molecular docking study of Co (II), Cu (II), and Zn (II) mixed ligand complexes. Crystals 2023;13:118.
6. Hansen S, Jensen K, Baun A. Nano risk cat: a conceptual tool for categorization and communication of exposure potentials and hazards of nanomaterials in consumer products. J Nanoparticle Res 2017;19.
7. Lu Z, Van Horn W, Chen J, Mathew S, Zent R, Sanders C. Bicelles at low concentrations. Mol Pharm 2012;9:752—61.
8. Zhang W, Sun J, He Z. The application of open disk-like structures as model membrane and drug carriers. Asian J Pharm Sci 2013;8:143—50.
9. Buzea C, Pacheco I, Robbie K. Nanomaterials and nanoparticles: sources and toxicity. Biointerphases 2007;2:17—71.
10. Lozano-Pérez AA, Pagán A, Zhurov V, Hudson SD, Hutter JL, Pruneri V, et al. The silk of gorse spider mite tetranychus lintearius represents a novel natural source of nanoparticles and biomaterials. Sci Rep 2020;10:18471.
11. Hoover M, Myers D, Cash LJ, Guilmette R, Kreyling W, Oberdorster G, et al. Radiation safety aspects of nanotechnology (No. LA-UR-15-21975). Los Alamos, NM, US: Los Alamos National Laboratory (LANL); 2017.
12. Duffin R, Mills N, Donaldson K. Nanoparticles — a thoracic toxicology perspective. Yonsei Med J 2007;48:561—72.
13. Al-Fakeh MS, Al-Otaibi NF. Nd_2O_3, Cr_2O_3, and V_2O_3 nanoparticles via calcination: synthesis, characterization, antimicrobial and antioxidant activities. J Nanotechnol 2022;2022:7794939—15.
14. Li Y, Cheng Y, Xu T. Design, synthesis and potent pharmaceutical applications of glycodendrimers: a mini review. Curr Drug Discov Technol 2007;4:246—54.
15. Cheng Y, Wang J, Rao T, He X, Xu T. Pharmaceutical applications of dendrimers: promising nanocarriers for drug delivery. Front Biosci 2008;13:1447—71.
16. Goldberg M, Langer R, Jia X. Nanostructured materials for applications in drug delivery and tissue engineering. Biomater Sci Polym Edition 2007;18:241—68.
17. Naito M, Yokoyama T, Hosokawa K, Nogi K. Nanoparticle technology handbook. Amsterdam, Netherlands: Elsevier; 2018.
18. Singh J, Dutta T, Kim K, Rawat M, amddar P, Kumar P. Green synthesis of metals and their oxide nanoparticles: applications for environmental remediation. J Nanobiotechnol 2018;16:84.
19. Wang P. Nanoscale biocatalyst systems. Curr Opin Biotechnol 2006;17:574—9.
20. Zhang L, Gu F, Chan J, Wang A, Langer R, Farokhzad O. Nanoparticles in medicine: therapeutic applications and developments. Clin Pharmacol Theraputics 2008;83:761—9.
21. Dorner L, Cancellieri C, Rheingans B, Walter M, Kägi R, Schmutz P, et al. Cost-effective sol—gel synthesis of porous CuO nanoparticle aggregates with tunable specific surface area. Sci Rep 2019;9:11758.
22. Assaouka HT, Daawe DM, Fomekong RL, Nsangou IN, Kouotou PM. Inexpensive and easily replicable precipitation of CuO nanoparticles for low temperature carbon monoxide and toluene catalytic oxidation. Heliyon 2022;8:e10689.
23. Bepari RA, Bharali P, Das BK. Synthesis of nanoscale CuO via precursor method and its application in the catalytic epoxidation of styrene. RSC Adv 2022;12:6044—53.
24. Hajipour A, Mohammadsaleh F, Sabzalian M. Copper-containing polyvinyl alcohol composite systems: preparation, characterization and biological activity. J Phys Chem Solid 2015;83:96—103.
25. Un Nisa Z, Tashfeen A. *Para*-aminobenzoic acid-A substrate of immense significance. Mini-Reviews Org Chem 2020;17:686—700.
26. Kratky M, Konecna K, Janousek J, Brablikova M, Jandourek O, Trejtnar F, et al. 4-Aminobenzoic acid derivatives: converting folate precursor to antimicrobial and cytotoxic agents. Biomolecules 2020;10.
27. Chen C, Ma C, Chan R, Ou H, Xie H, Wong A, et al. A long lasting sunscreen controversy of 4-aminobenzoic acid and 4-dimethylaminobenzaldehyde derivatives resolved by ultrafast

spectroscopy combined with density functional theoretical study. Phys Chem Chem Phys 2020;22:8006—20.
28. Al-Fakeh MS, Alsaedi RO, Aldoghaim M, Ibrahim ABM, Mostafa AM. Nickel oxide nanoparticles derived from coordination polymer of PVA and aminobenzoic acid derivative: synthesis, characterization and antimicrobial activity. Polymers 2025;17:301.
29. Al-Fakeh M, Alminderej F. New method for the preparation and biological activity of CuO nanoparticles from a mixed PVA and 2-Aminobenzothiazole complex. Int J Chemtech Res 2018;11:2455—9555.
30. Reena P, Joema SE, Darling DA, Sindhusha S, Abith M, Girisun TCS. Systematic discussion on nonlinear optical and antibacterial activity of guanidinium benzene-1, 2-dicarboxylate (GUBD) single crystal for laser and biomedical applications. J Mater Sci Mater Electron 2021;32:25545—60.
31. Saravanan M, Hari BV, Brzeziński M, Gonciarz W, Potheher IV, Girisun TS. Improved antibacterial activity and biocompatibility of porphyrin functionalized metal decorated reduced graphene oxide. Surf Interfaces 2024;46:103932.
32. Archana N, Vijayasri M, Dayanidhi K, Parthiban S, Girisun TS. Hybrid tin (IV)-based heterocyclic compound with halogen acids: crystal structure, DFT, Hirshfeld surface analysis and antioxidant investigations. Next Mater 2025;8:100814.
33. Hendrawan H, Khoerunnisa F, Sonjaya Y, Purti A. Poly (vinylalcohol)/glutaraldehyde/premna oblongifolia merr extract hydrogel for controlled-release and water absorption application. Mater Sci Eng 2019;509:012048.
34. Roik N, Belyakova L. IR spectroscopy, X-Ray diffraction and thermal analysis studies of solid "β-cyclodextrin — *Para*-aminobenzoic acid" inclusion complex. Phys Chem Solid State 2011:12.
35. Al-Fakeh M, Alsaedi R. Synthesis, characterization, and antimicrobial activity of CoO nanoparticles from a Co (II) complex derived from polyvinyl alcohol and aminobenzoic acid derivative. Sci World J 2021;2021:1—11.
36. Al-Fakeh M. Facile preparation of a nanostructured silver oxide from a mixed ligand coordination polymer: characterization and biological activity. Adv Res 2017;10:1—8.
37. Al-Fakeh M. Synthesis and characterization of coordination polymers of 1,3-Di(4- Pyridyl)-Propane and 2-Aminobenzothiazole with Mn(II), Co(II), Cu(II) and Ni(II) ions. J Chem Pharmaceut Res 2018;10:77—83.
38. Al-Fakeh MS, Allazzam GA, Yarkandi NH. Ni (II), Cu (II), Mn (II), and Fe (II) metal complexes containing 1, 3-Bis (diphenylphosphino) propane and pyridine derivative: synthesis, characterization, and antimicrobial activity. Int J Biomater 2021;1:4981367—12.
39. Siddaiah T, Ojha P, Kumar G, Ramu C. Structural, optical and thermal characterizations of PVA/MAA:EA polyblend films. Mater Res 2018;21. https://doi.org/10.1590/1980-5373-mr-2017-0987.
40. Gainar A, Stevens J, Suljoti E, Xiao J, Gonlak R, Aziz E, et al. The structure of *P*-aminobenzoic acid in water: studies combining UV-Vis, NEXAFS and RIXS spectroscopies. J Phys Conf 2016:712.
41. Ogwuegbu MC, Olatunde OC, Onwudiwe DC, Mthiyane DM, Fawole OA, Onwudiwe DC. Green synthesis of CuO and Ce-doped CuO nanoparticles using aqueous extract of yam peel and their antimicrobial properties. Hybrid Adv 2024;7:100335.
42. Al-Fakeh MS. Synthesis, thermal stability and kinetic studies of copper (II) and cobalt (II) complexes derived from 4-aminobenzohydrazide and 2-mercaptobenzothiazole. Eur Chem Bull 2020;9:403—9.
43. Coats A, Redfern J. Kinetic parameters from thermogravimetric data. Nature 1964;201:68—9.
44. Horowitz H, Gershon M. A new analysis of thermogravimetric traces. Anal Chem 1963;35:1464—8.
45. Klug H, Alexander L. X-ray diffraction procedures for polycrystalline and amorphous materials. Hoboken, NJ, USA: Wiley; 1954:716 p.
46. El-Ghoul Y, Al-Fakeh MS, Al-Subaie NS. Synthesis and characterization of a new alginate/carrageenan crosslinked biopolymer and study of the antibacterial, antioxidant, and anticancer performance of its Mn (II), Fe (III), Ni (II), and Cu (II) polymeric complexes. Polymers 2023;15:2511.
47. Armentano I, Arciola C, Fortunati E, Davide F, Mattioil S, Amoroso C, et al. The interaction of bacteria with engineered nanostructured polymeric materials: a review. Sci World J 2014;2014:1—18.
48. Gao W, Thamphiwatana S, Angsantikul P, Zhang L. Nanoparticle approaches against bacterial infections. Wiley Nanomed Nanobiotechnol 2014;6:532—47.
49. Luan B, Huynh T, Zhou R. Complete wetting of graphene by biological lipids. Nanoscale 2016;8:5750—4.
50. Zakharova O, Godymchuk A, Gusev A, Gulchenko S, Vasyukova I, Kuznetsov D. Considerable variation of antibacterial activity of Cu nanoparticles suspensions depending on the storage time, dispersive medium, and particle sizes. BioMed Res Int 2015;2015:1—11.
51. Leung Y, Ng A, Xu X, Shen Z, Gething L, Wong M, et al. Mechanisms of antibacterial activity of MgO: non-ROS mediated toxicity of MgO nanoparticles towards Escherichia coli. Small 2013;10:1171—83.
52. Andersson D, Hughes D, Kubicek-Sutherland J. Mechanisms and consequences of bacterial resistance to antimicrobial peptides. Drug Resist Updates 2016;26:43—57.